JOURNAL OF GEOPHYSICAL RESEARCH, VOL. 99, NO. B9, PAGES 18,159–18,173, SEPTEMBER 10, 1994

Nucleation and growth of faults in brittle rocks

Ze'ev Reches
Department of Geology, Hebrew University, Jerusalem, Israel

David A. Lockner
U.S. Geological Survey, Menlo Park, California

Abstract. We present a model for the nucleation and growth of faults in intact brittle rocks. The model is based on recent experiments that utilize acoustic emission events to monitor faulting processes in Westerly granite. In these experiments a fault initiated at one site without significant preceding damage. The fault propagated in its own plane with a leading zone of intense microcracking. We propose here that faults in granites nucleate and propagate by the interaction of tensile microcracks in the following style. During early loading, tensile microcracking occurs randomly, with no significant crack interaction and with no relation to the location or inclination of the future fault. As the load reaches the ultimate strength, nucleation initiates when a few tensile microcracks interact and enhance the dilation of one another. They create a process zone that is a region with closely spaced microcracks. In highly loaded rock, the stress field associated with microcrack dilation forces crack interaction to spread in an unstable manner and recursive geometry. Thus the process zone propagates unstably into the intact rock. As the process zone lengthens, its central part yields by shear and a fault nucleus forms. The fault nucleus grows in the wake of the propagating process zone. The stress fields associated with shear along the fault further enhance the microcrack dilation in the process zone. The analysis shows that faults should propagate in their own plane, making an angle of 20°-30° with the maximum compression axis. This model provides a physical basis for "internal friction," the empirical parameter of the Coulomb criterion.

Introduction

The mechanisms of fault nucleation and fault propagation in rocks have been enigmatic since Coulomb proposed the basis for faulting theory in 1773. Nucleation was first attributed to an incipient flaw which grows in its own plane [*Griffith*, 1920]. However, stress analyses and experimental works indicate that an incipient shear fault in rock could not grow and propagate in its own plane [*Brace and Bombolakis*, 1963]. Then, it was postulated that faults formed by the coalescence of arrays of microcracks or damage points which existed before faulting initiated [*Brace et al.*, 1966; *Scholz*, 1968; *Peng and Johnson*, 1972; *Hallbauer et al.*, 1973; *Ashby and Hallam*, 1986; *Horii and Nemat-Nasser*, 1985]. Recent experimental observations however, indicated that preyielding microcracks in a homogeneous granite have little effect on the geometry and location of the future fault [*Lockner et al.*, 1991; *Lockner and Byerlee*, 1993; *Moore et al.*, 1990]. We propose here that a fault nucleates by local interaction among a few microcracks and that it propagates into the unfaulted regions by inducing microcrack growth at its front.

Paper number 94JB00115.
0148-0227/94/94JB-00115$05.00

The importance of preexisting flaws in controlling tensile strength of brittle materials was first recognized by *Griffith* [1920]. *McClintock and Walsh* [1962] extended the Griffith theory to shear failure under compression. The resulting modified Griffith theory was successful at reproducing the Coulomb failure criterion which predicts that faulting occurs when

$$\tau = C + \mu \sigma_n$$

where τ denotes shear stress across the fault plane, C is rock cohesion, μ is coefficient of internal friction, and σ_n is normal stress across the fault. C and μ are experimentally determined material parameters. The modified Griffith theory did not, however, consider the well-documented experimental result that faulting is preceded by growth of microcracks which are subparallel to the maximum compressive stress [*Brace and Bombolakis*, 1963; *Tapponnier and Brace*, 1976; *Madden*, 1983; *Peng and Johnson*, 1972]. Further, experiments and model calculations [*Brace and Bombolakis*, 1963; *Horii and Nemat-Nasser*, 1985] indicated that shear cracks in brittle rocks will not grow in their own plane. In a few experiments, shear cracks were found to grow by in-plane propagation [*Reches*, 1988; *Petit and Barquins*, 1988], but this growth does not occur in brittle rocks or by Griffith's mechanism [*Reches*, 1988].

The observations of intense microcracking prior to faulting led to the concept that brittle rocks yield due to distributed microcrack damage. It was assumed that the

microcracks form independently of each other until they reach a critical density and then they coalesce unstably. The coalescence occurs along a microcrack array which is oriented obliquely to σ_1, and within this array the rock fails through buckling of the intercrack columns [*Peng and Johnson*, 1972; *Horii and Nemat-Nasser*, 1985; *Ashby and Hallam*, 1986; *Ashby and Sammis*, 1990]. *Brace et al.* [1966] interpreted acoustic emission data to suggest that in advanced stages of faulting experiments the microcracks concentrated within a restricted zone and that macroscopic yielding eventually occurred along this zone. This notion that microcracks are organized along the future fault zone was also used by *Peng and Johnson* [1972], who mapped the microcracks in faulted granite samples, by *Hallbauer et al.* [1973], and by *Ashby and Hallam* [1986]. *Du and Aydin* [1991] modeled the interactions within a long array of microcracks. The main objectives of the present study are to specify the processes of nucleation which lead to the formation of a crack array and the manner in which this array propagates to form a fault zone.

Nucleation and Growth of Faults in Westerly Granite

Lockner et al. [1991, 1992a] have presented experimental observations of quasi-static fault growth in Westerly granite and Berea sandstone. By using an array of piezoelectric transducers, they recorded the arrival times of acoustic emission (AE) events which indicate the impulsive growth of microcracks. The arrival times were then inverted to obtain three-dimensional locations of the events that occurred during fault nucleation and growth. Results from a triaxial experiment on Westerly granite are shown in Figure 1. The following general stages of fault development were observed: (1) Prior to fault nucleation (not shown), AE activity was low and uniformly distributed throughout the sample; these early events reflected homogeneous microcracking during the loading phase. There was no obvious precursor in AE event locations to indicate either the time or the position of the nucleation zone, although a relative increase in the number of

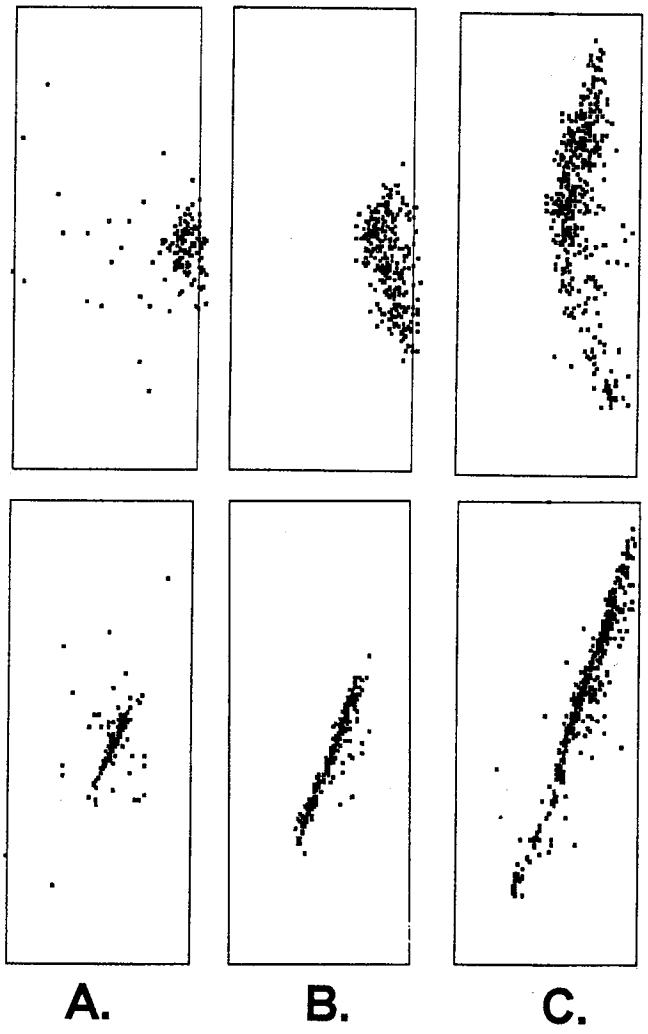

Figure 1. Computer-generated display of over 1200 acoustic emission (AE) events in Westerly granite experiment: (a) nucleation; coalescence of AE activity forming a distinct nucleus of the fault on the sample surface and (b) and (c) fault growth; the fault propagates away from the nucleation site within its own plane. Sample dimensions were 19.1 cm length and 7.6 cm diameter. Confining pressure was 50 MPa. The AE sources are plotted in paired views which are rotated 90° to each other. Bottom plots are viewed along the strike of the eventual fault; top plots view developing fault surface face on.

large-amplitude events was recorded [*Lockner et al.*, 1991; *Lockner and Byerlee*, 1993]. (2) A sudden increase of AE corresponded to fault nucleation at the sample surface (Figure 1a). The fault plane inclination was already apparent in this stage. The fault propagated in its plane as mixed shear modes II and III (Figures 1b and 1c). The AE activity was most intense at the front of the propagating fault and activity decreased noticeably after the front passed. (3) The fault front moved through the rock as a distinct entity, with dimension of 1 to 3 cm in the direction of propagation.

These results provide a number of important clues regarding the process of brittle faulting. The prenucleation AE locations indicate that in a homogeneous rock, microcracks are sparse and microcrack damage remains diffuse until near peak stress. Then, following nucleation, the fault controls the location of further microcrack growth. This damage is concentrated at the advancing fracture tip in a pattern that resembles the process zone postulated for shear along a preexisting fault plane [*Rice*, 1980]. While the granite sample had no preexisting fault, the observed structure of the propagating damage zone indicates that Rice's process zone may also be applied to fault propagation in intact rocks.

A central result is the observation that a fault nucleated at one site and propagated from it without significant preceding damage. There are no indications that the fault surface formed by coalescence of a preexisting, randomly distributed arrays of microcracks as proposed previously [*Peng and Johnson*, 1972; *Horii and Nemat-Nasser*, 1985; *Ashby and Hallam*, 1986]. Thus we infer that the advancing fracture itself induces organized damage which is restricted to its own plane. This model is supported by the density and orientation of microcrack damage associated with a propagating shear fracture as observed in thin sections [*Moore and Lockner*, 1994].

A Model for Fault Nucleation and Growth

Approach

We propose here a model for faulting of brittle rocks that is based on microcrack interactions in the experiments described above. A key aspect of the model comes from

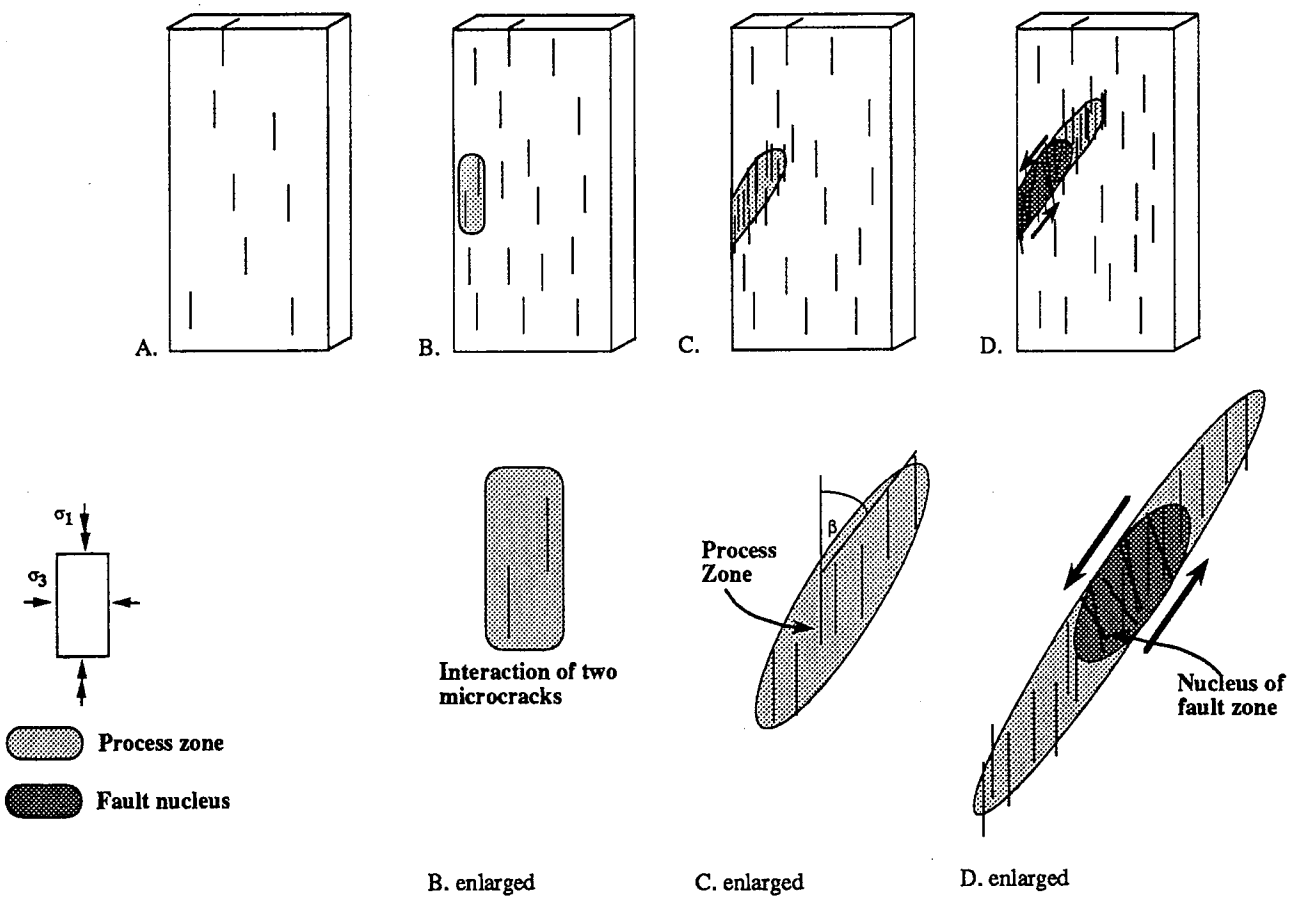

Figure 2. The idealized model for the faulting of a brittle plate by mutual enhancement of cracking. Plate is under biaxial loading. (a) Preloading: sites of potential microcracks are randomly distributed (thin lines). (b) After substantial loading: many dilated microcracks in random distribution (thick lines); the local stresses induced by the dilation of a crack (in marked rectangle) could trigger its neighbor which is on the verge of opening. (c) At about peak strength. Nucleation and local increase of crack density lead to the development of a process zone (dotted region) by the dilation of potential microcracks due to tension induced by a dilated crack. (d) Fault zone: the weakened tail of the process zone yields by crushing, buckling, and rotation of microblocks.

the stress calculations for a crack in an elastic solid. These calculations predict that the region of maximum tension induced by an open crack is not in the crack plane but is inclined at an angle of at least 30° with respect to the crack [*Lawn and Wilshaw*, 1975; *Horii and Nemat-Nasser*, 1985; *Pollard and Segall*, 1987; *Reches and Lockner*, 1990]. We first present the idealized model and then show that the stress field associated with microcracks controls the angle for reinforced crack interaction and the geometry of the fault surface.

The model is derived for an idealized configuration of a thin brittle plate that contains many microcracks (Figure 2). The plate is biaxially loaded by uniform remote stresses of $\sigma_1 > \sigma_3$; σ_3 is constant, and σ_1 increases until faulting occurs. During early loading some microcracks dilate and alter the stress field in their proximity. Because the dilating cracks are sparse, they do not yet affect each other (Figure 2a). As the load increases, the density of the dilated cracks increases, and locally a crack that otherwise would be stable is caused to yield due to the tensile stress induced by its dilated neighbor. We propose that in the highly stressed plate, the dilation of one crack can induce the dilation of closely spaced neighboring cracks that were themselves on the verge of opening. This damage region with dense interacting cracks is regarded here as the process zone (Figure 2c). The process zone extends by inducing tensile stresses across new cracks that are on the verge of opening. As the process zone lengthens, its central part is weakened by the dense cracking and eventually yields by shear (Figure 2d). This locus of sheared, rotated and crushed microblocks is the fault nucleus that develops into the fault zone (Figure 2d). The process zone continues to propagate and to lead the fault zone until the sample is bisected.

Formation of the Process Zone

Microcracking. The growth of dilational microcracks in brittle rocks that are subjected to compressive confining pressure has been attributed to local loading associated with microscopic structural features. The common features, described in the appendix, include the mismatch of grain boundaries, differences in elastic moduli between minerals, intracrystalline flaws, and shear along grain boundaries [*Tapponnier and Brace*, 1976; *Ashby and Sammis*, 1990]. These structural features apply inhomogeneous loading to the interior of the dilating cracks [*Lawn and Wilshaw*, 1975; *Ashby and Hallam*, 1986]. The exact stress analysis of such internal loading may be complicated and will differ from one microscopic geometry to another [*Lawn and Wilshaw*, 1975]. In the appendix we adopt the approach of *Lawn and Wilshaw* [1975] that the inhomogeneous loading associated with microcracking may be represented by uniform pressure inside the microcrack. We thus assume that the linear and parallel microcracks in the idealized model (Figure 2) can be analyzed in terms of cracks subjected to uniform internal pressure P (equation (A3), appendix). This assumption provides a unified representation to the various mechanisms of microcracking as described in the appendix.

Induced dilation of microcracking. The stress fields associated with crack dilation have been studied in several works. Here we use the formulation of *Pollard and Segall* [1987]. They derived the stress fields of mode I, mode II, and mode III cracks that are embedded in a linear, elastic solid; the formulations are for plane strain and plane stress conditions.

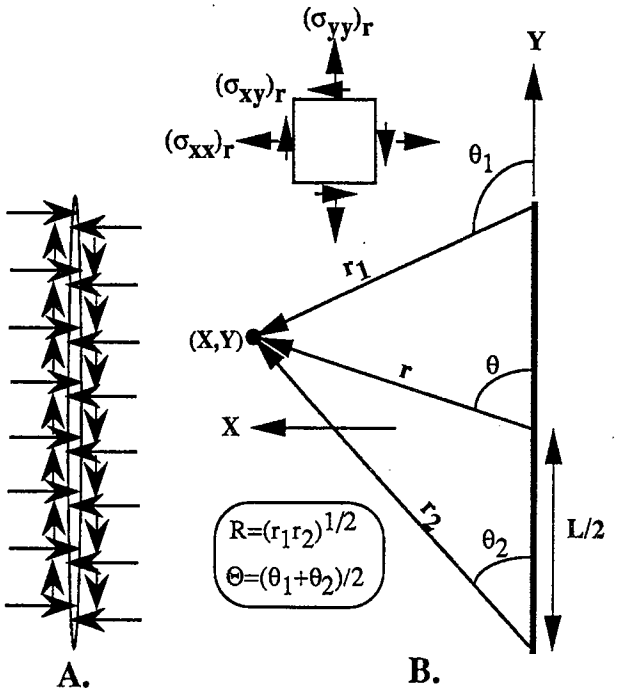

Figure 3. (a) Crack with mode I and mode II driving stresses and (b) geometry, coordinate system and stress convention used in the present calculations [after *Pollard and Segall*, 1987].

The stresses at a point are the superposition of the remote stresses of the loading system and the local stresses induced by the three modes of cracking. Figure 3 displays the coordinates and sign convention for a crack with mode I and mode II displacement under plane-strain conditions. The stresses at a point (X, Y) due to these displacements are [*Pollard and Segall*, 1987, equations 8.44],

$$\sigma_{XX} = (\sigma_{XX})_r + \Delta\sigma_I [(r/R)\cos(\theta - \Theta) - 1 + (L/2)^2 (r/R^3) \sin\theta \sin 3\Theta] + \Delta\sigma_{II} [(L/2)^2 (r/R^3) \sin\theta \cos 3\Theta] \quad (1a)$$

$$\sigma_{XY} = (\sigma_{XY})_r + \Delta\sigma_{II} [(r/R)\cos(\theta - \Theta) - 1 - (L/2)^2 (r/R^3) \sin\theta \sin 3\Theta] + \Delta\sigma_I [(L/2)^2 (r/R^3) \sin\theta \cos 3\Theta] \quad (1b)$$

$$\sigma_{YY} = (\sigma_{YY})_r + \Delta\sigma_I [(r/R)\cos(\theta - \Theta) - 1 - (L/2)^2 (r/R^3) \sin\theta \sin 3\Theta] + \Delta\sigma_{II} [2(r/R)\sin(\theta-\Theta) - (L/2)^2 (r/R^3) \sin\theta \cos 3\Theta] \quad (1c)$$

where $(\sigma_{XX})_r$, $(\sigma_{YY})_r$ and $(\sigma_{XY})_r$ are the remote stresses, $\Delta\sigma_I$ and $\Delta\sigma_{II}$ are the driving stresses associated with mode I and mode II displacements, respectively, L is the crack length, and the angles θ and Θ and the distances r and R are defined in Figure 3b.

We first consider the stress field induced by the dilation of a crack A and its effect on a closed crack B that is on the verge of opening; in the idealized case, crack B is parallel and equal in length to A (Figure 4). Following the appendix, we assume that the isolated crack A dilates when

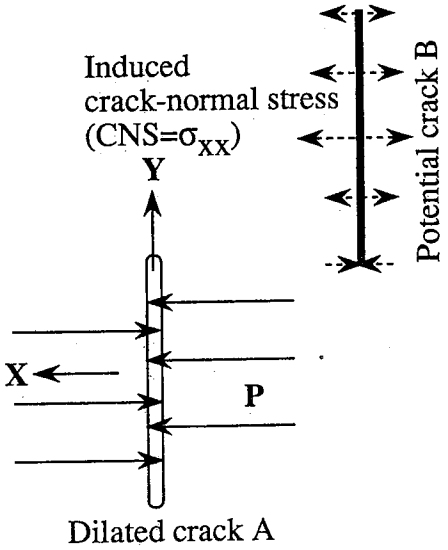

Figure 4. Schematic presentation of the crack normal stresses induced on a closed crack B by the dilation of crack A (mode I). Crack A is subjected to internal pressure *P*.

subjected to internal pressure *P*. The dilation of A generates a local, nonuniform stress field which induces stresses on neighboring cracks. The dilation of crack B is most significantly affected by the intensity of the σ_{XX} component of the induced stress field, which is normal to the crack (Figures 3 and 4). Thus only the σ_{XX} component is displayed here, and it is termed crack normal stress, or CNS (Figure 4).

The intensity of CNS is calculated by substituting $(\sigma_{XX})_r = 0$ (no remote stresses), $\Delta\sigma_I = P = 1$ (mode I dilation due to internal pressure, appendix), and $\Delta\sigma_{II} = 0$ (no crack parallel shear) into equation (1a),

$$\mathrm{CNS} = \Delta\sigma_I \left[(r / R)\cos(\theta - \Theta) - 1 + (L / 2)^2 (r / R^3) \sin\theta \sin 3\Theta\right] \quad (2)$$

The intensity field of CNS according to the last equation is shown in the left side of Figure 5. By using $\Delta\sigma_I = P = 1$, CNS is normalized with respect to the internal pressure *P* (see the appendix for the magnitude of *P*).

Figure 5 shows that CNS is tensile in two regions off the tips of crack A (upper left and lower left, Figure 5) and that it is compressive along the center of the crack (center left, Figure 5). As the CNS field is nonuniform, a crack of finite length will be subjected to various intensities of CNS along its strand (e.g., crack B in Figure 4). We thus calculate average magnitude of the crack normal stresses, $\mathrm{CNS}_{\mathrm{average}}$. The $\mathrm{CNS}_{\mathrm{average}}$ at a point (x_c, y_c) is the integral of σ_{XX} over the area of a potential crack centered at (x_c, y_c). σ_{XX} is calculated from the last equation, and the potential crack is taken as parallel to the dilating isolated crack and equal to it in length (area). For a unit width of the model plate,

$$\mathrm{CNS}_{\mathrm{average}} = \int_{y_c - L/2}^{y_c + L/2} \sigma_{XX}\, dy$$

where L is the crack length. $\mathrm{CNS}_{\mathrm{average}}$ is integrated numerically according to the last equation and by using the expression for σ_{XX} in (2). The intensity map of the $\mathrm{CNS}_{\mathrm{average}}$ is plotted in the right side of Figure 5.

Consider now two cracks at the proximity of A which are on the verge of opening (cracks 1 and 2 on right side of Figure 5). Crack 1 is subjected to tensile $\mathrm{CNS}_{\mathrm{average}}$, and thus its tendency to dilate is enhanced; crack 2 is subjected to compressive $\mathrm{CNS}_{\mathrm{average}}$, and thus its tendency to dilate is diminished. We regard the intensity of $\mathrm{CNS}_{\mathrm{average}}$ as a good approximation for the effect of crack A on the potential cracks 1 and 2.

$\mathrm{CNS}_{\mathrm{average}}$ is a function of the angle θ_1 and the distance r_1 from the tip of crack A (Figure 3b). For constant distance r_1, $\mathrm{CNS}_{\mathrm{average}}$ passes through a point of maximum tension at an angle of $\theta_1 = \theta_M$. The loci of these points with maximum tension were calculated for $0 < r_1 < 3L$ and for $0 < \theta_1 < \pi$. These loci are plotted as curve M in upper right side of Figure 5 and in Figure 6. Cracks centered on curve M are most likely to dilate due to the dilation of crack A. The result is that new cracks that are induced to open by the stress field associated with crack A are stepped relative to A and are most likely to be centered on curve M.

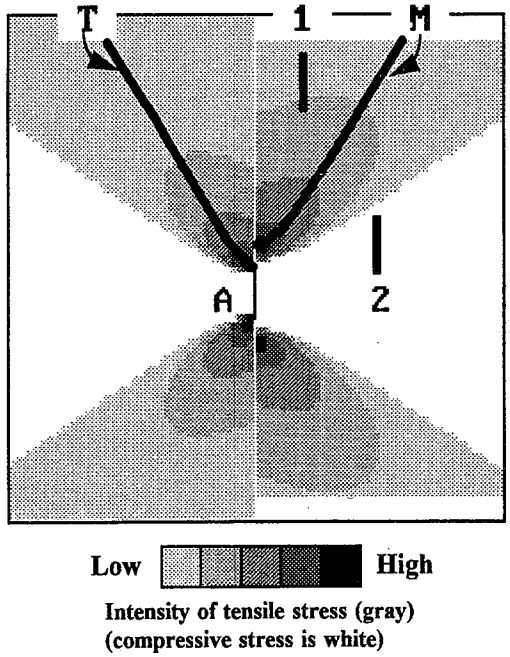

Figure 5. The crack normal stress (CNS = σ_{XX}) associated with the dilation of a mode I crack (crack A in center). The dilation is under uniform internal pressure without remote stresses (see text). The intensity of the tensile CNS is shown by the gray scale; zones with compressive CNS are white. (left) CNS (σ_{XX}) associated with crack A dilation; curve T connects the points with maximum intensity of this stress component for a given distance from the tip of A. (right) $\mathrm{CNS}_{\mathrm{average}}$ acting on a crack equal in length and parallel to crack A (calculated with equation (2) from the stress field shown on left). Curve M connects the points with maximum intensity of $\mathrm{CNS}_{\mathrm{average}}$ for a given distance from the tip of crack A. Curves T and M are similar in shape but slightly displaced. Cracks 1 and 2 are potential cracks at the proximity of the dilating crack A. Note that crack 1 is subjected to tensile $\mathrm{CNS}_{\mathrm{average}}$ whereas crack 2 is subjected to compressive $\mathrm{CNS}_{\mathrm{average}}$ (in white zone).

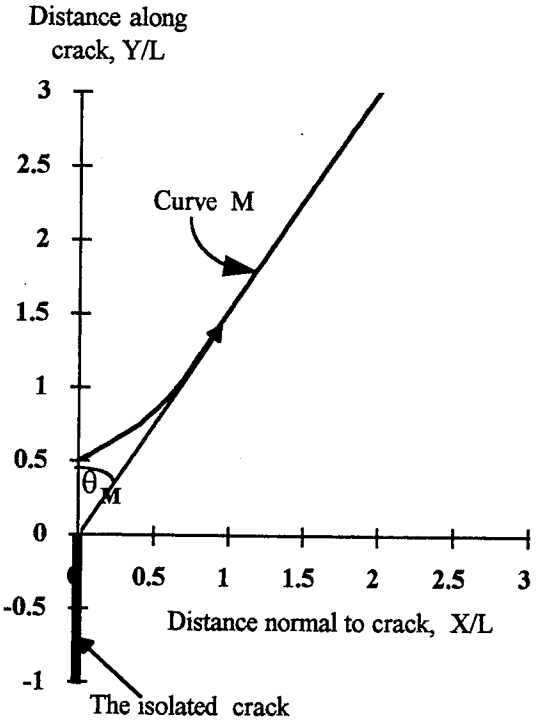

Figure 6. Details of the M curve as it extends from the tip of crack A (details of the right side of Figure 5).

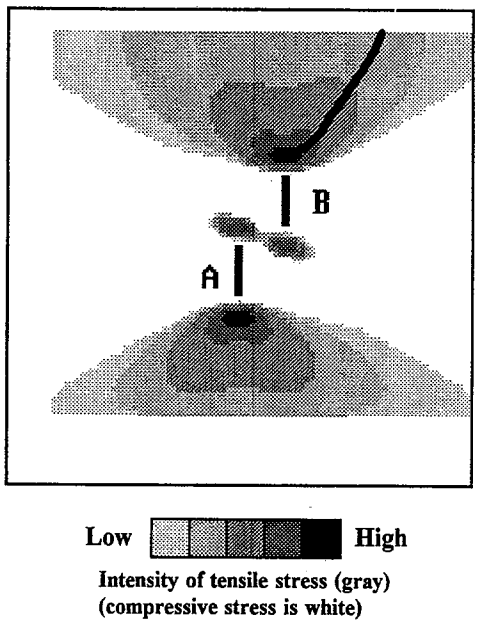

Figure 7. The average crack normal stress ($CNS_{average}$) associated with the dilation of two parallel mode I cracks (cracks A and B). Both cracks are on the M curve of each other, and they dilate under uniform internal pressure without remote stresses. The intensity of the tensile CNS is shown by the gray scale; zones with compressive CNS are white. The M curve of both cracks is plotted with respect to crack B.

The recognition that an induced crack is off the axis of the first crack is central to our model since the orientation of the eventual shear fracture is controlled by this off-axis constructive crack interaction.

Stepped cracks and the geometry of the process zone. We propose that fault nucleation could initiate from a pair of interacting, stepped cracks (Figure 2b). Such a pair could propel nucleation if it could induce the dilation of additional potential cracks in an unstable fashion. To examine this possibility, the combined $CNS_{average}$ of two stepped cracks that lie along each others M curve was calculated (Figure 7). The field of the combined $CNS_{average}$ of two cracks (Figure 7) is similar in shape to $CNS_{average}$ field of one crack (right side of Figure 5). The M curve of the two combined cracks is essentially identical to curve M of a single crack (Figure 7 and right side of Figure 5). Thus a third crack C, that is dilated by the combined $CNS_{average}$ of cracks A and B, would have similar geometry with respect to B, as B has with respect to A. In other words, the array of cracks A, B, C and so on, maintains the same oblique arrangement of similar geometry.

Further, when C is located with respect to B in the same position as B with respect to A, then the combined $CNS_{average}$ on C due to A and B is larger by 20-70% with respect to the $CNS_{average}$ on B due to A alone (Figure 8). Therefore the third stepped crack would be more easily dilated then the second crack. This result indicates an unstable process in a highly stressed sample. In such a sample many potential cracks are on the verge of dilation, and thus a pair of neighboring stepped cracks is likely to activate crack C leading to a sequence of dilation of other cracks. This dilation of a crack array would rapidly develop into unstable faulting (Figures 2d and 9). If the sample is not highly stressed, pairs of cracks might be favorably oriented to activate each other, but they could not nucleate faulting as the neighboring microcracks are unlikely to be sufficiently stressed to continue the process. We thus conclude that a system of stepped cracks within a sample on the verge of yielding would extend itself unstably by inducing cracks arranged in similar geometry.

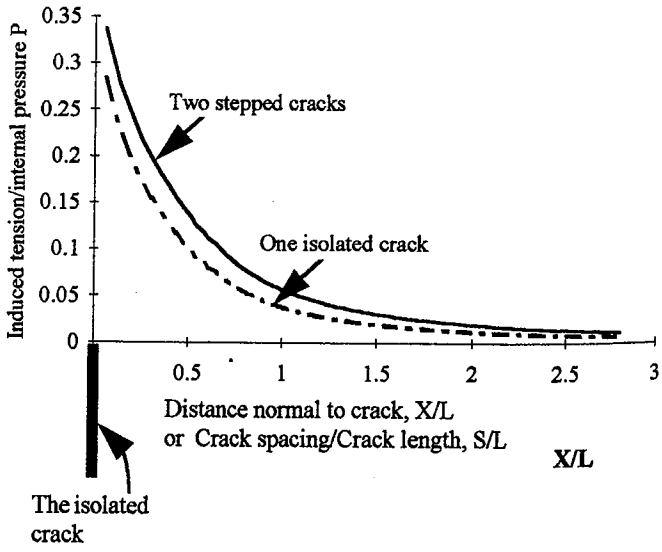

Figure 8. Intensity of the induced crack normal stress ($CNS_{average}$) along the M curve for one isolated crack (crack A in Figure 5) and two stepped cracks (cracks A and B in Figure 7). The induced stress is shown as fraction of the internal pressure *P*. Note that for $X/L > 1$ the tension induced by two cracks is significantly larger in relative magnitude then the tension induced by one crack.

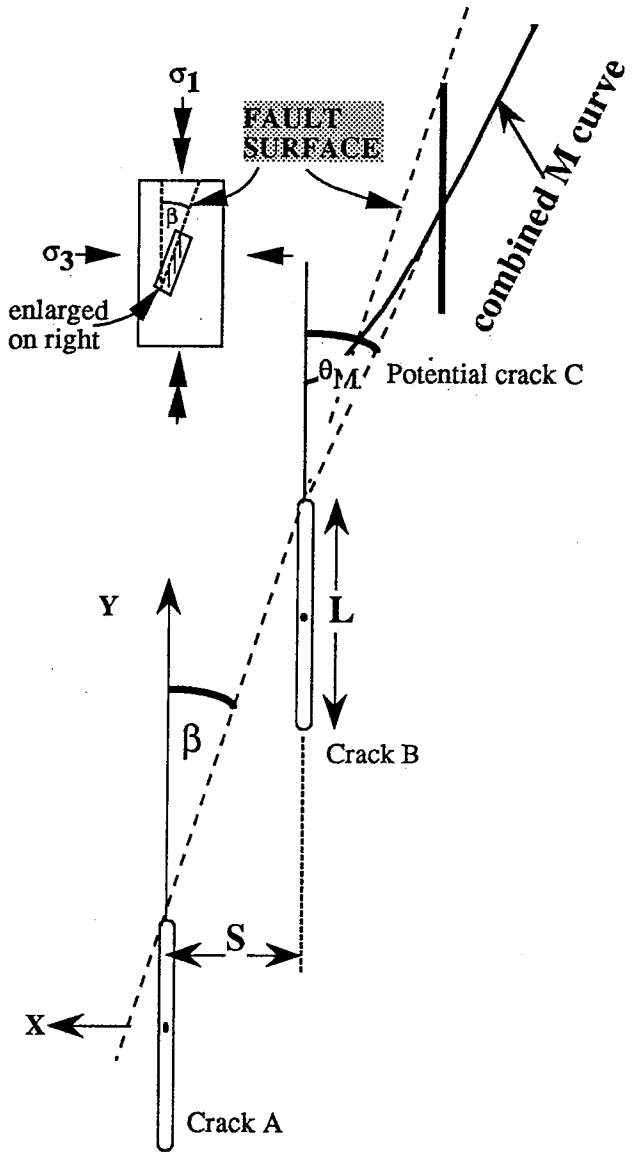

Figure 9. The geometry of three mode I cracks that mutually enhance their dilation. They are located on the M curve of each other. The expression of the fault inclination β is presented in equation (3).

If the process zone extends in a recursive style as shown above, the geometry of an ideal two-crack unit controls the geometry of the process zone and the fault plane. The fault plane in the two-dimensional model is the line which connects the tips of two or more cracks which are centered on the M curve of each other (Figure 9). The angle β between the fault plane and σ_1, the axis of maximum compression, can be derived from Figure 9,

$$\beta = \tan^{-1}\{[2(S/L)\sin\theta_M]/[\sin\theta_M + 2(S/L)\cos\theta_M]\}$$

where S is the crack spacing, L is the crack length and θ_M is the angle between σ_1 and the line that connects the tip of crack A and the center of crack B (Figure 6). Note that crack B is centered on the M curve (Figure 7). The angle θ_M ranges from 65° to 34° as determined numerically from the M curve (Figure 6). θ_M was substituted into the last equation to obtain fault inclination β as a function of spacing/length ratio, S/L (Figure 10). The last equation indicates that for the known range of θ_M, β ranges from 0° for $S/L = 0$ to 34° for $S/L > 5$ (Figure 10).

The range of β can be further restricted. First, the tension induced by a dilating crack ($CNS_{average}$) decays approximately as the reciprocal of the distance from the dilating crack (equation (1a)). Figures 8 and 10 show that the induced tension decays exponentially with increasing S/L. For $S/L \approx 2$ the induced tension is ≈ 1% of the internal pressure P required to dilate an isolated crack. We estimate that 1% of induced tension only marginally affects the potential crack, and we select $S/L \approx 2$ as the maximum ratio for crack interaction. This selection implies an upper bound of $\beta \approx 30°$ (Figure 10).

Second, the pattern of potential cracks in a brittle rock is likely to be related to the grain boundaries [*Tapponnier and Brace*, 1976]; thus a reasonable spacing/length ratio of potential cracks is around 1. This estimate is supported by measurements of microcrack densities. *Hadley* [1975] (as presented by *Madden* [1983]), and *Lockner et al.* [1992b] presented crack density D in terms of (number of cracks)/(unit area). Assuming random distribution of the microcracks, one can show that

$$S = \sqrt{1/D}$$

and thus

$$S/L \approx \sqrt{1/(DL^2)}$$

These relations were applied to the data of *Hadley* [1975] and *Lockner et al.* [1992b]. We found that in the undeformed samples, S/L ranges from 1 to 4 and in the

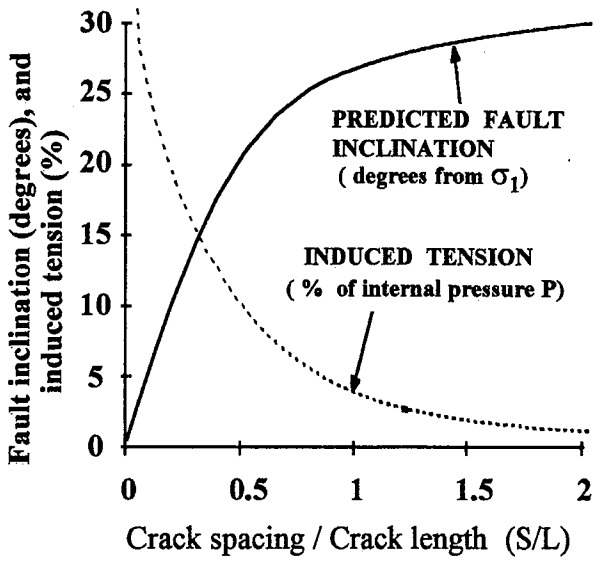

Figure 10. Fault inclination β (solid line) predicted by the mutual enhancement cracking model and the intensity of the induced tensile stress (dashed line) along the M curve. Crack spacing, crack length and the angle β are defined in Figure 9. β is displayed in degrees; the induced tensile stress is displayed as the ratio of $CNS_{average}$ to the internal pressure (in percent). The angle β vanishes as the spacing-to-length ratio S/L vanishes and its maximum value is 34° for $S/L > 5$; these angular relations are also apparent on curve M in Figure 6.

fractured samples S/L is roughly 0.35 to 1 [*Lockner et al.*, 1992b] . We thus estimate that $S/L = 0.5$ is a lower bound at the time of yielding; this bound implies that $\beta > 20°$ (Figure 10).

Figure 10 provides a robust result: in a brittle homogeneous rock the angle between a fault and the axis of maximum compression is within the range of $20° < \beta < 30°$. β can be expressed through the Coulomb criterion as $\beta = \pm (45° - \varnothing/2)$, where $\varnothing$ is the angle of internal friction [*Jaeger and Cook*, 1984]. The deduced limits on β yield $50° > \varnothing > 30°$, in agreement with countless experimental results.

Growth of the Fault Zone

Our experiments revealed intensive AE activity in front of the propagating fault (Figure 1). These observations, supported by the thin section analysis of *Moore and Lockner* [1994], were interpreted as indicating that the propagation is controlled by a process zone followed by shear along the newly formed fault zone (Figure 2d). The effects of this shear on the faulting processes are evaluated by calculating the stresses associated with a fault that is represented here by a mode II fracture.

The calculations for the fault are for $\sigma_{1r}/\sigma_{3r} = 6$, a typical stress state in the present granite faulting experiments [*Lockner et al.*, 1991]; σ_{1r} and σ_{3r} are applied by the loading apparatus, and both are compressive (Figure 11a). The intensity of the tensile σ_3 at the proximity of a slipping fault is plotted in Figure 11b; σ_3 is the sum of the remote stresses (associated with the loading system in Figure 11a) and the local stresses induced by the fault zone (equation (1)). The σ_3 component is plotted because the present model is based on dilating microcracks. Figure 11b displays two regions in which σ_3 is tensional: lobe A in front of the fault and lobe B to the left of the fault tip for left-lateral shear. The length of lobe A is 10-15% of the length of the fault, and it correlates in location and extent with the process zone. As the microcracks in the process zone are parallel to σ_1 (Figure 2) and as σ_1 in lobe A is subparallel to the remote σ_{1r} (Figure 11b), the stresses of lobe A enhance the tensile stresses acting on the microcracks in front of the fault zone. The effect of lobe A is independent of the tension induced by the microcracks on each other (described above), and it amplifies the tendency of the process zone to propagate in its own plane. Tensile microcracking that correlates well with lobe A has been shown experimentally by *Petit and Barquins* [1988].

Lobe B is the site of the well-documented tensile cracks that form close to the tips of a fault [*Brace and Bombolakis*, 1963; *Ashby and Hallam*, 1986; *Horii and Nemat-Nasser*, 1986]. These tensile cracks, sometimes called wing cracks, are usually stable in that their extension requires an increase of the loading stress. If the fault does not propagate into the uncracked host material, the wing cracks grow longer and wider with loading [e.g., *Brace and Bombolakis*, 1963; *Horii and Nemat-Nasser*, 1986].

The process that is considered here differs from the wing cracking. The fault of Figure 11 propagates, and both lobes A and B move with the fault (and the leading process zone). It is not clear if the fault is "pulled" by the process zone or if the fault "pushes" the process zone. In either case, as lobe B advances with the fault tip its tensile cracks are left behind and enter the compressive conditions associated with the central part of the fault (Figure 11b). Therefore for a propagating fault the tensile stresses of lobe B exist momentary at any given location. This momentary tension is restricted to one side of the crack: when the left-

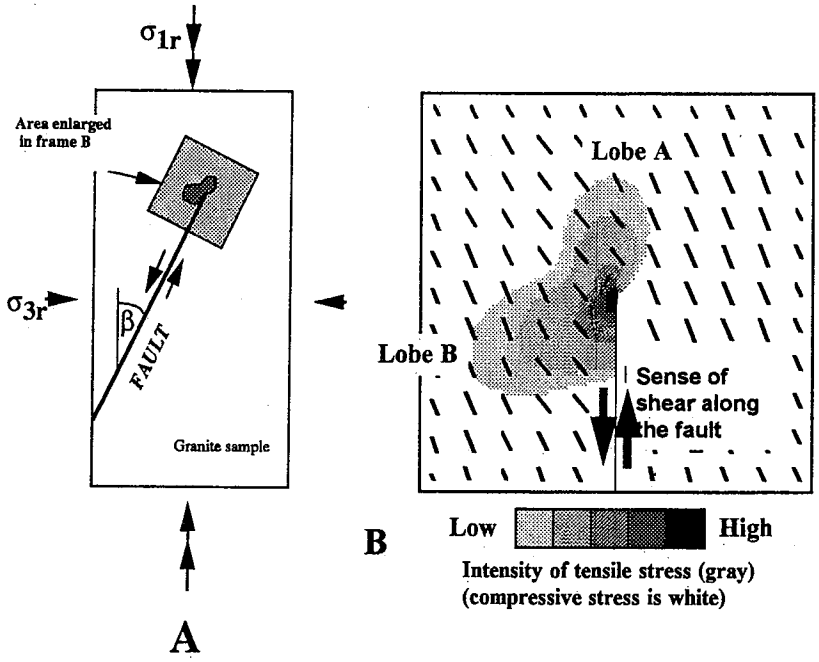

Figure 11. Stresses associated with the slip along a left-lateral fault (mode II fracture). (a) The sample setup. The dotted region at the tip of the fracture is displayed in Figure 11b. The sample is subjected to compressive remote stresses of $\sigma_{1r}/\sigma_{3r} = 6$ and $\beta = 26.5°$; $\beta = 26.5°$ is the predicted fault inclination for spacing/length of 1 (Figure 10). (b) The intensity of the tensile stresses σ_3 (gray scale); regions of compressive σ_3 are white; solid, short lines indicate the local orientation of maximum compression axis. Note the two lobes of tensile stress lobe A in front of the shear crack and lobe B on its left side (see text).

lateral crack of Figure 11b propagates upward, the left block is expected to be more damaged by microcracks of lobe B than the right block. Opposite relations would exist for a right-lateral crack. This prediction has been confirmed for both laboratory faults [*Moore and Lockner*, 1994] and field observations [*Scholz et al.*, 1993]. In conclusion, the tensile stresses developed close to the tip of a propagating fault zone (mode II fracture) enhance the tensile conditions in the leading process zone and intensify its propagation (lobe A); they also cause damage on one side of the propagating fault (lobe B). This prediction of asymmetric damage is tested in the next section.

Experimental Observations in Light of the Model

Fault Nucleation

The experiments reported here provide key observations with regard to fault nucleation and growth in granite. We use the distribution of the AE events in these experiments to represent the distribution of microcracking events during faulting (following *Brace et al.* [1966], *Lockner et al.* [1991], and others).

The prefaulting AE events in the experiments display no apparent localization pattern [*Lockner et al.*, 1991]. The only noticeable deviation from randomness is the relative deficiency of events close to the loading pistons, probably due to local higher confinement. The AE events during nucleation display a different pattern. The locations of 100 AE events that occurred before, during, and after nucleation in Westerly granite are plotted in Figure 12 (test G3 of *Lockner et al.* [1992a]). The events are separated into five groups of 20 consecutive events. While the events of the first group (Figure 12a) are dispersed, the events of the following four groups are clustered along a distinct inclined zone (Figures 12b-12e). Thus nucleation occurred during the transition from the first to the second group.

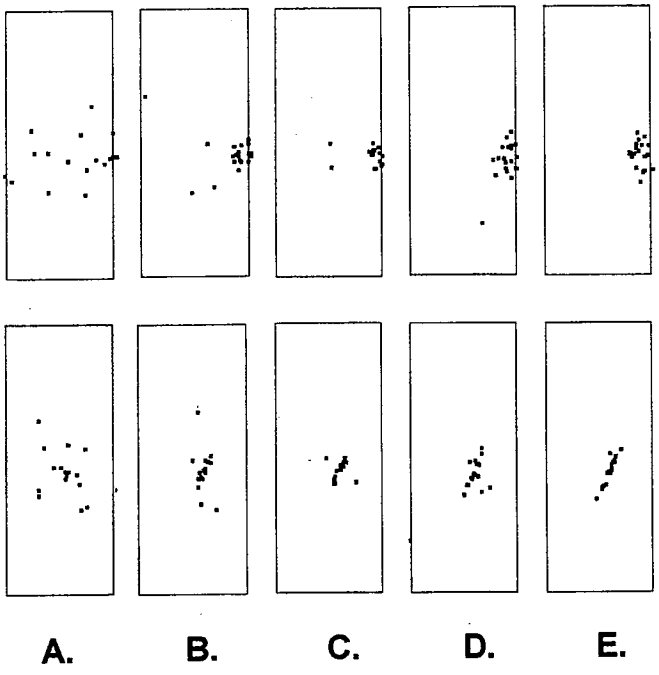

Figure 12. Locations of 100 acoustic emission (AE) events which occurred before, during and after nucleation in G3 test, Westerly granite [*Lockner et al.*, 1992a]. Legend is same as in Figure 1. (a)-(e) Plots of five groups of AE events, 20 events in each. Note the closely spaced events in Figures 12b-12e.

Another effective way to recognize the nucleation is by using a geometric parameter termed here as the containment sphere. A containment sphere is defined for a group of N consecutive AE events; its center is (X_c,Y_c,Z_c) and its radius is R_c, where $X_c = \Sigma X_i/N$, $Y_c = \Sigma Y_i/N$ and $Z_c = \Sigma Z_i/N$, Σ indicates summation for $i = 1...N$, (X_i,Y_i,Z_i) is the location of the ith AE event, and $R_c = \Sigma r_i/N$ where r_i is the distance from (X_i,Y_i,Z_i) to (X_c,Y_c,Z_c). An illustration for the containment sphere is shown in Figure 13a for 20 events under two-dimensional conditions (Z_c = const). It is apparent from Figure 13a that the volume of a containment sphere is a sensible approximation for the volume occupied by the group of events.

We calculated the containment spheres for the 100 consecutive AE events presented in Figure 12. The containment spheres were calculated for groups of 20 consecutive events; the first group is for $i = 1,2,\cdots,20$, second group is for $i = 2,3,\cdots,21$ and the last group is for $i = 80,81,\cdots,100$ (in a similar style to running average). Figure 13b displays the calculated volumes of these containment spheres with respect to the time of the first event in each group. The volumes of the first 17-18 groups are 20-25 cm^3 whereas the volumes of the following groups are about 5 cm^3 or less (Figure 13b). This abrupt volume drop reflects the transition from sparse cracking at random distribution to localized cracking within a process zone approximately 3 cm^3 in volume (Figure 13b). This is the nucleation stage.

It is unknown what controls the volume of the process zone. We think that it is related to the size of the microcracks and the length of the fault, and we thus anticipate a larger process zone will be associated with a larger fault.

Figure 13 shows that the nucleation stage is short: it takes less than five AE events (out of the 13,500 well-located events) to establish the transition from random distribution to well-organized pattern. Note also that all the 100 events of Figure 12 occurred above 0.995 of the maximum load in this experiment. If the experiment had been stopped a few events before the observed nucleation, the location and the orientation of the future fault could not be recognized. This observation is in complete agreement with the nucleation process of the present model.

The propagation stage which follows the nucleation is characterized by AE activity within a thin zone (1-5 mm) (Figures 12b-12e). The density of microcracks associated within this zone is 100 to 1000 times the density of prenucleation microcracking. Thus the sparse uniformly distributed prenucleation cracks cannot control, or even effect, the dense cracking of the propagating fault. This thin zone of intense microcracking corresponds to the process zone of the model (Figure 2b), which eventually transforms into a fault zone (Figure 2d).

Asymmetric Damage

The present model predicts that the tensile stresses developed close to the tip of a propagating fault zone would cause more damage on one side of the propagating fault

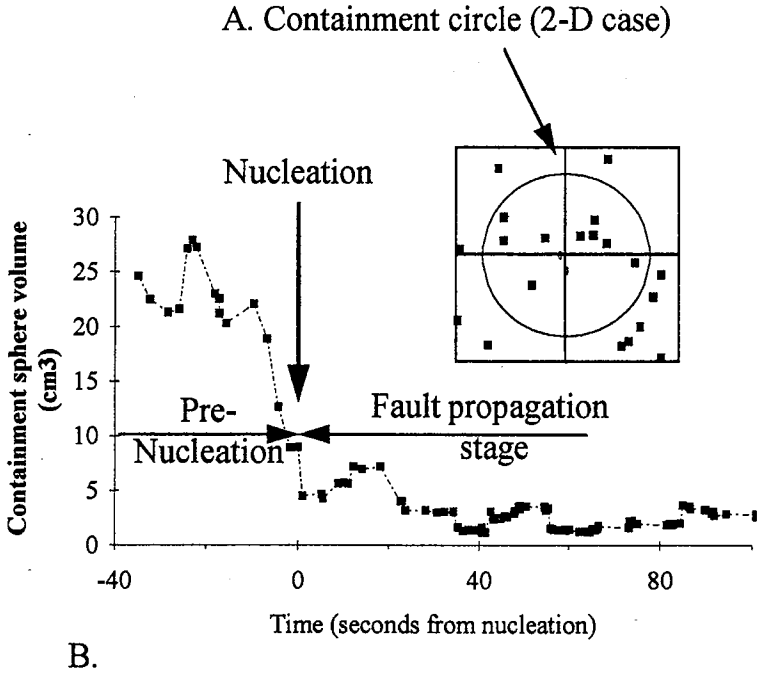

Figure 13. Geometry of the nucleation process in experiment G3 of Westerly granite presented by means of containment spheres of acoustic emission AE events (see text). (a) The containment sphere for 20 events under two-dimensional conditions for which the sphere is reduced to a circle. Solid squares are locations of the events; the circle was calculated according to the text. (b) Volumes of the containment spheres for groups of 20 consecutive events out of the 100 events displayed in Figure 12. The groups of 20 AE events were calculated in a style similar to running average, and 100 events have 100 containment spheres (see text). The horizontal axis indicates the elapsed time during the experiment; this time is controlled by the rate of AE events, and it has no physical significance (see experimental description in text).

(Figure 10). This prediction of asymmetric damage of the fault margins is now compared with the microcracks at the proximity of the fault in experiment G3 of Westerly granite (Figure 14). Figure 14a includes a cross section normal to the fault with a nucleation zone (large circle) and propagation direction (two opposing arrows) (Figure 14a is similar in position to the lower part of Figure 1). Postfailure displacement of about 2 mm occurred along the fault, and an ≈1-mm-wide gouge zone formed. The sample was impregnated with blue epoxy under vacuum; the epoxy penetrated into the gauge zone and into the microcracks close to it. The open S shape of the fault reflects disintegration of the sample upon the release of the confining pressure. Figure 14b is a map of the microcracks at the proximity of the fault as traced on photographic enlargements of a thin section. A total of 1174 cracks were traced with trend distribution as in Figure 14c. Cracks shorter than ≈ 100 μm are inadequately represented due to resolution limits.

Figure 14 portrays that the microcracks at the proximity of the fault are subparallel to maximum compression axis (Figures 14a and 14c). The microcracks are concentrated along the fault zone and are less abundant at distances of ≈2 mm or more from the fault (Figure 14b). Further, more microcracks (894 cracks) appear on the left side of the fault than on the right side (280 cracks) (Figure 14b).

This damage asymmetry is not expected from the setup of the sample. The left side of the fault is closer to the loading end pieces than is the right side (Figure 14a). The region close to the loading end pieces is subjected to relatively high local confinement as is evidenced by the lack of local AE activity [*Lockner et al.*, 1991]. It is expected that, owing to this higher confinement, the left side would be less fractured than the right one. Thus the observed asymmetric damage of Figure 14b contradicts the confinement consideration. On the other hand, this damage asymmetry fits well the prediction of the present model: one side of a propagating fault should be more damaged than the other (Figure 11). According to this prediction, the propagation direction of a fault can be determined from the difference in crack distribution on both its sides.

Discussion

Faulting: Nucleation and Propagation of a New Crack Array Versus Coalescence of Prefaulting Crack Arrays

Two concepts central to the present model are that a fault nucleates within a small volume and that it propagates as a microcrack array into the unfaulted rock. These concepts are based on recent experiments which indicated that nucleation in Westerly granite occurs within a zone of 3 cm^3 in volume, at differential stress above about 0.995 of maximum load, and with no preceding development of an embryonic fault zone. These experiments, presented here and elsewhere (details are given by *Lockner et al.* [1991, 1992b]), provide continuous, nondestructive, and three-dimensional mapping of microcracking during a complete experiment. We regard these experiments as the most

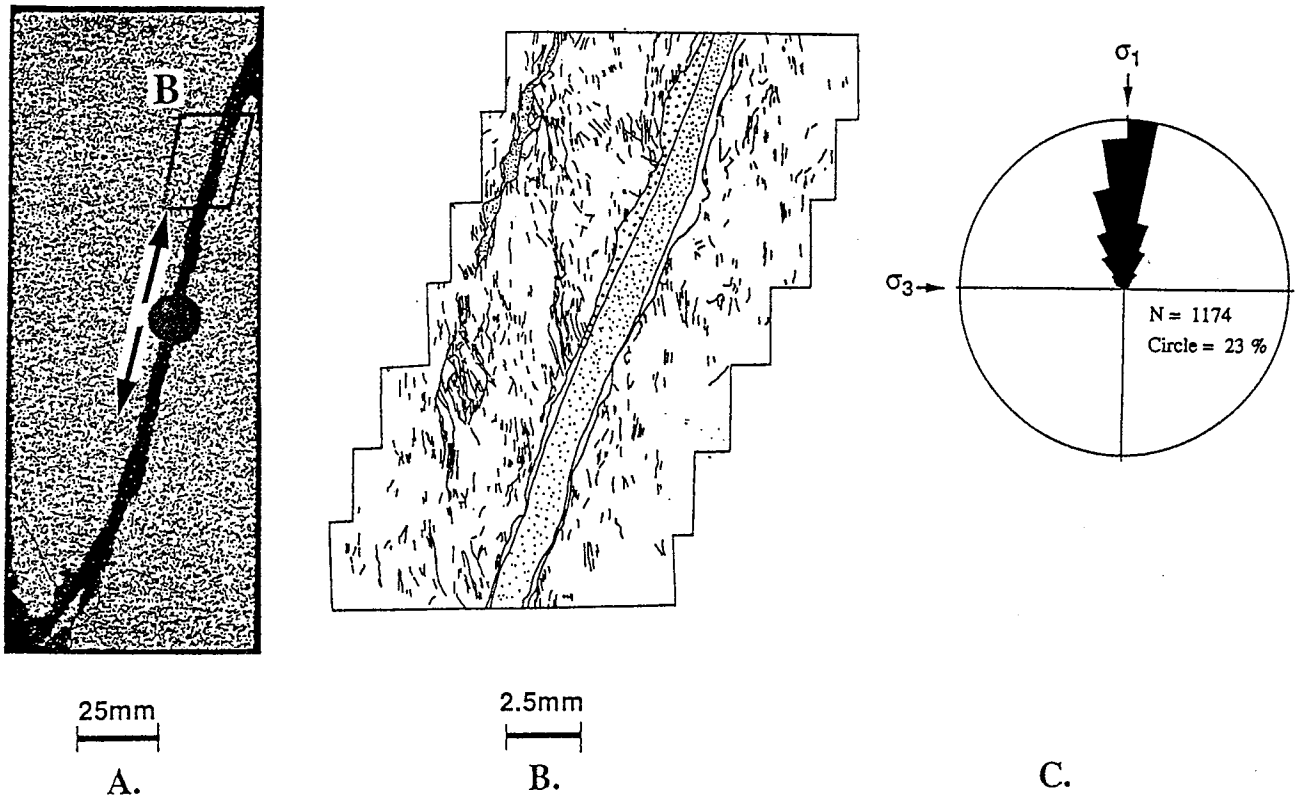

Figure 14. Microcracks at the proximity of the fault in experiment G3, Westerly granite [*Lockner et al.*, 1991]. Maximum compression is vertical. (a) Cross section normal to the sample in a similar orientation to the lower sections in Figure 1; the nucleation zone is marked by a circle, and the propagation direction appears by opposing solid arrows. Postfailure displacement of about 2 mm occurred along an ≈ 1-mm-wide gouge zone. (b) Microcracks at the proximity of the fault as traced on photographic enlargement of a thin section. (c) Trend distribution of the microcracks (with respect to maximum compression).

reliable in recognizing the details of nucleation and propagation processes. However, the dimensions of the experimental process zone or the fault nucleus probably reflect the sample dimensions, and they may differ under other conditions.

Previous microcrack models of faulting assumed, explicitly or implicitly, that faulting occurs by coalescence of microcracks which form prior to faulting [*Brace et al.*, 1966; *Peng and Johnson*, 1972; *Segall and Pollard*, 1983; *Hallbauer et al.*, 1973; *Horii and Nemat-Nasser*, 1985; *Ashby and Hallam*, 1986]. It was also suggested that the prefaulting microcracks are localized along the surface of the future fault [*Brace et al.*, 1966].

This view that microcracks outline the fault zone prior to faulting is not supported by observations made in the new experiments with AE control (see above and *Lockner et al.* [1991, 1992b]), or by the microscopic observations of experimentally faulted samples of Westerly and Barre granites conducted by *Moore et al.* [1990]. *Moore et al.* [1990, p. 11] concluded that "the patterns of microcracking in samples run to 90% and even 99% of the failure stress give no indication of the eventual position of the fault."

Microcrack arrays could also form by the development of a pervasive network of cracks and damage points prior to faulting. The suitable array could be established by coalescence of cracks from a dense yet random pattern. This concept implicitly requires that the density of cracking (or damage) away from the fault would be comparable to the density of cracking along the initial fault. This requirement contradicts field observations that unfaulted blocks are only slightly cracked or damaged away from the faults. This interpretation also contradicts the current experiments in which the AE density within the fault zone is 2-3 orders of magnitude larger than the density outside the zone (see above and *Moore and Lockner* [1994]). While a critical density of cracks is probably needed for fault nucleation, the prenucleation cracks are too sparse to control, or even affect, the dense cracking of the propagating fault.

It appears that the microcracking in the described granite experiments contradicts the conditions necessary to generate faults by coalescence of a prefaulting crack array. On the other hand, the experimental observations support the present concept that faults grow unstably from a nucleation site by mutual enhancement of microcrack dilation (Figure 2). *Petit and Barquins* [1988, 1990] reached similar conclusions following their experiments with slabs of modeling plastic. They used an experimental configuration similar to that of Figure 10, and they observed a microcrack array developing in front of the fault. However, the fault did not grow or propagate in their experiments, probably due to the relatively high strength of the plastic.

Pattern of Microcracks

The present model is based on the interaction among two or three planar and parallel microcracks that have equal

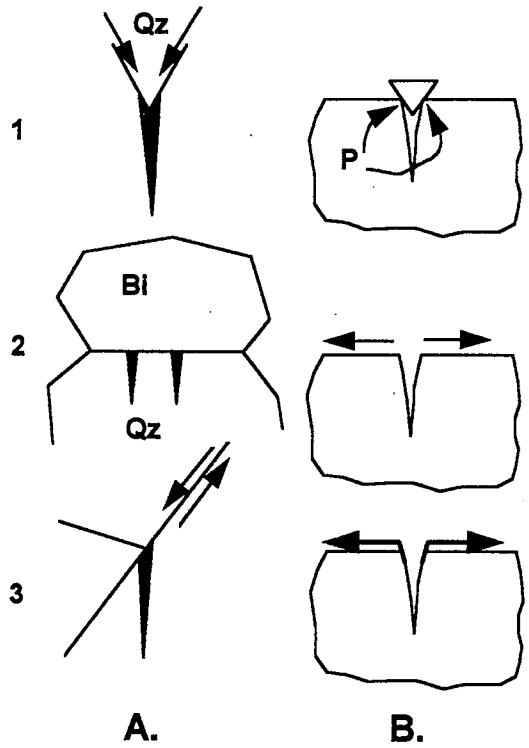

Figure 15. Schematic presentation of the dominant microcracking mechanisms in brittle rocks [after *Tapponnier and Brace*, 1976; *Kranz*, 1979]. (a) Geometry of the three cracking mechanisms: (1) wedging of a grain or the contact between two grains by an intruding rigid grain, (2) cracking due to difference in the elastic moduli of two adjacent and bonded crystals Bi is a biotite grain; Qz is a quartz grain, and (3) slip along micro fractures with tensile cracking at its ends ("wing crack"). (b) Idealized configurations of the nonuniform loading associated with the mechanisms in Figure 15a: (1) concentrated force at the points p, (2) shear stresses acting parallel to the grain surface leading to crack widening, and (3) concentrated forces applied at the fracture tip to generate the crack.

length. Previous studies referred to other crack configurations: *Ashby and Hallam* [1986] investigated the growth of wing cracks, *Du and Aydin* [1991] analyzed interaction within an array of tensile cracks, and *Sammis and Ashby* [1986] studied crack growth from circular inclusions and holes. *Horii and Nemat-Nasser* [1985, 1986] investigated an infinitely long array of equally spaced, identical shear fractures which extend by wing cracking. They solved for fracturing associated with an array of well-constrained geometry, and their solutions provided some impressive fits to experimental results [*Horii and Nemat-Nasser*, 1985, Figures 15 and 16].

Choosing a well-constrained array geometry provides a rigorous basis for the analysis, yet such "choices are not guided by any actual microcrack observations." [*Horii and Nemat-Nasser*, 1985, p. 3116]. Microscopic studies indicate that microcrack dilation under confining pressure may be attributed to local loading associated with mismatch of grain boundaries, differences in elastic moduli between minerals, intracrystalline flaws, and shear along grain boundaries (appendix). However, we have not seen an attempt to quantify the dilation mechanisms. We chose to replace the nonspecific, inhomogeneous loading of microcracking (Figure 15) by a uniform pressure P (Figure 16b).

Interestingly, the analyses of microcrack interaction by the different approaches provide similar results. *Horii and Nemat-Nasser* [1985] predicted fault inclinations of 29°-36° or as small as ≈20° under low confinement. *Du and Aydin* [1991] derived fault inclination of ≈ 28° from a crack array arrangement. We predicted as described above that fault inclination should be 20°-30°. This general similarity of the predicted fault angles despite the different analytical approaches is not fortuitous and not so surprising. Stress analysis indicates that the region of maximum tension induced by an open crack is not in the crack plane; rather, it is inclined at an angle of at least 30° (Figure 5) [*Lawn and Wilshaw*, 1975; *Pollard and Segall*, 1987]. This stress field controls the angle for reinforced crack interaction and tension enhancement. We suggest that regardless of the detailed geometry of the microcrack arrays, they behave as arrays of dilating tensile cracks, inducing similar stress fields (for example, the stress field in Figure 5). Therefore the simple tensile crack configuration analyzed here can approximately represent the complex cracking processes in front of a fault.

Conclusions

The experimental observations indicate that in brittle homogeneous rock a fault nucleates at a point without apparent precursors and that the fault propagates in its own plane by means of a leading process zone. We derived a model based on mutual enhancement of microcracking due to stress induction. The analysis predicts that a fault should propagate within its own plane making an angle of 20°-30°

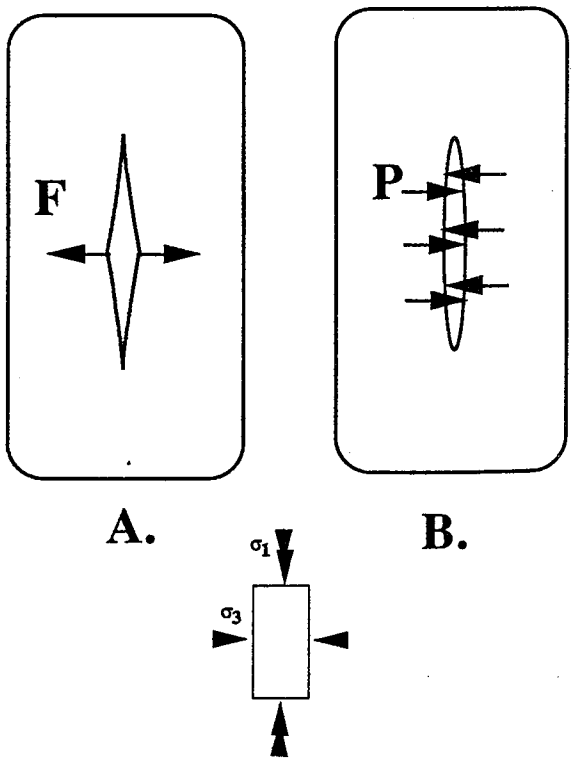

Figure 16. The cracking mechanisms of Figure 15 idealized as mode I crack loaded by (a) an intra-crack force F at its center or by (b) uniform pressure P.

with the axis of maximum compression. This prediction is in agreement with the bulk of experimentally formed faults and provides a physical mechanism for the fault inclination determined by the Coulomb faulting criterion.

Appendix

The main objective of this appendix is to obtain a simple crack form which may approximately represent the various microcracking mechanisms in brittle rocks. Microcracking has usually been attributed to the inhomogeneous structure of brittle rocks [*Tapponnier and Brace*, 1976; *Kranz*, 1979]. One common cracking mechanism is the wedging of a grain or the contact between two grains by an intruding rigid grain (A1 in Figure 15a). Quartz grains are likely to serve as the rigid wedges in granites. In the ideal configuration the intruding wedge applies loading forces at a point of contact (B1 in Figure 15a). Another mechanism (A2 in Figure 15a) represents cracking due to the difference in the elastic moduli of two adjacent and bonded crystals. Under a given state of stress the two crystals will extend differently due to the difference in their elastic moduli and crystallographic orientation. The grain which extends more (e.g., the biotite in A2, Figure 15a), applies shear along the grain contacts leading to cracking of the grain which extends less (e.g., the quartz in A2, Figure 15a). A third mechanism includes slip along microfractures that causes tensile cracking at the termination zones of the slipping fracture (A3 in Figure 15a) [*Lawn and Wilshaw*, 1975].

We now examine the common properties of these mechanisms in terms of fracture mechanics. The stress intensity factor associated with a mode I crack in a two-dimensional infinite body may be expressed in several forms. For a crack subjected to a uniform tensile stress normal to it, σ_L, [*Lawn and Wilshaw*, 1975],

$$K_I = \sigma_L \sqrt{\pi L/2} \qquad (A1)$$

For a crack subjected to uniform internal pressure P, (Figure 16b),

$$K_I = P \sqrt{\pi L/2} \qquad (A2)$$

To apply the uniform stress distributions to the nonuniform loading in Figure 15, we idealize these cracks as continuous mode I cracks loaded by intracrack force F. This force acts along a line at the center of the crack (Figure 16a). *Lawn and Wilshaw* [1975, p. 65] considered a crack inside an infinite plate which is subjected to point line forces F at (±x,0). The stress intensity factor K_I for the case of x = 0 and $\sigma_3 = 0$ is [*Lawn and Wilshaw*, 1975, equation 3.25]

$$K_I = F / \sqrt{\pi L/2} \qquad (A3)$$

where F is measured in Newton per unit thickness of the plate. The last two equations are analogous: they express K_I in terms of either internal force (F in (A3)) or internal pressure (P in equation (A2)). Equating (A2) and (A3) yields

$$P = 2F/(\pi L). \qquad (A4)$$

This equation shows that the intracrack force F may be expressed in terms of an equivalent internal loading. Finally, we accept that a crack dilates when $K_I = K_{IC}$ where K_{IC} is the fracture toughness.

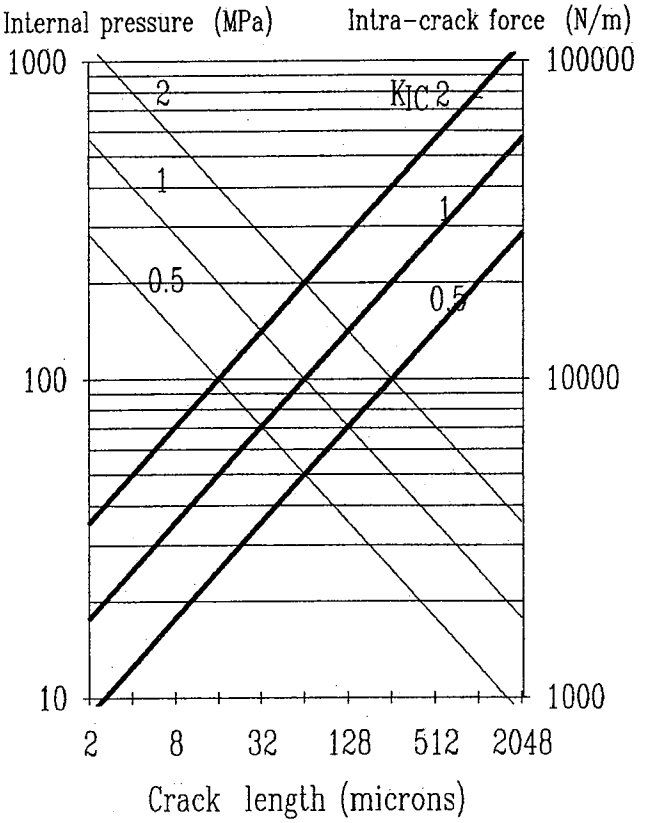

Figure A1. The intracrack force F (equation (A3)) (heavy lines) and the internal pressure P (equation (A2)) (light lines) required to dilate tensile cracks of the marked length. Plots are for K_{IC} = 0.5, 1, and 2 MPa $m^{1/2}$ as marked on the lines.

Figure A1 displays the magnitudes of intra-crack force F (equation (A3)) and the internal pressure P (equation (A2)) for cracks of 2 μm < L < 2048 μm. The values of F and P are plotted for K_I = 0.5, 1, and 2 MPa $m^{1/2}$, the range of fracture toughness of the common minerals in granites. Crack growth by internal point loads is stable as F increases with increasing crack length (Figure A1). On the other hand, P decreases with crack length, indicating unstable crack growth (similarly to the unstable cracking under remote tension, (A1)). The internal pressure P can be used as equivalent to the intracrack force F (equation (A4)). For example, a crack which is 32 μm long within a mineral of which K_{IC} = 1 MPa $m^{1/2}$, could be dilated either to $P \approx$ 141 MPa or $F \approx$ 7900 N/m; equivalent relations can be found for other cracks. Confining pressure may be superposed on the solutions, utilizing the additive nature of the stress intensity factor.

Hadley [1975] measured the density of microcracks in Westerly granite for three loading levels: preloading, loading to 65% of yielding strength and postfailure. The median crack length in the preloading stage is 3-10 μm and the median crack length is 30-100 μm in the postfailure sample (Figure A2). Cracks longer than 1000 μm are essentially absent even in the failed sample. Similar results were recently reported by *Lockner et al.* [1992b] and *Moore and Lockner* [1994]. These measured lengths may be used to bound the magnitude of F and P of Figure A1. The

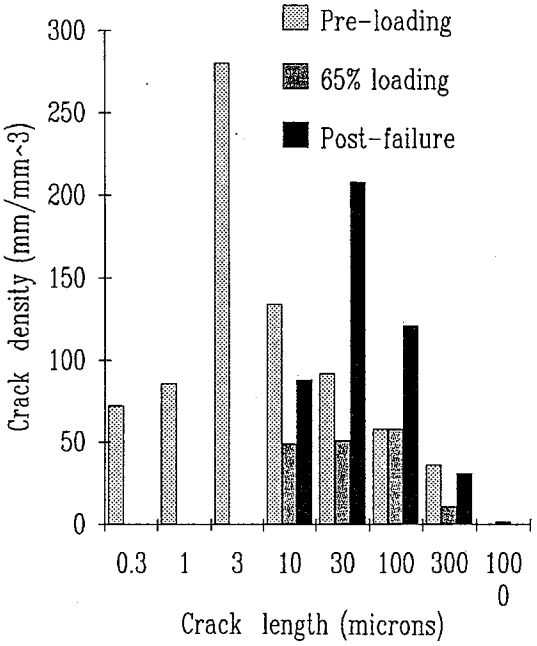

Figure A2. Crack length populations in Westerly granite (measurements by *Hadley* [1975]). Crack densities are shown for preloading, loading to 65% of yielding strength and postfailure.

general absence of cracks longer than 1000 μm provides an upper bound on the intracrack force: $F < 20{,}000$ N/m, with equivalent internal pressure of 12 MPa (above confinement). Determining the lower bound is less clear. In the preloaded sample fewer than 10% of the measured cracks are longer than 30 μm (Figure A2). Thus we deduced that the highest loads on the original rocks could dilate cracks of $L < 30$ μm; this implies $F < 3425$ N/m and $P \approx 73$ MPa for the weak minerals (Figure A1).

In summary, first, we assert here that the various cracking mechanisms in rocks (Figure 15), may be represented by a simple mode I crack subjected to intracrack, nonuniform load (Figure 16c). Second, following the approach of *Lawn and Wilshaw* [1975], the nonuniform load associated with these mechanisms can be replaced by a uniform pressure P inside the crack. These two deductions are utilized in the stress analysis in the text.

Acknowledgments. We benefited from discussions with Jim Byerlee, Jim Dieterich, Mel Friedman, Leonid Germanoviz, Ze'ev Riess, Paul Segall, Bob Simpson, Dave Stearns, Mark Zoback, and the late Yuri Liberman. The comments of Atilla Aydin, John Logan and Charles Sammis and the suggestions of William Durham, the associate editor, and two anonymous reviewers contributed significantly to the paper. The research was done during the sabbatical of the senior author supported by the Tectonophysics Branch, U.S. Geological Survey, Menlo Park, California.

References

Ashby, M. F., and S. D. Hallam, The failure of brittle solids containing small cracks under compressive stress states, *Acta Metall., 34*, 497-510, 1986.

Ashby, M. F., and C. G. Sammis, The damage mechanics of brittle solids in compression, *Pure Appl. Geophys., 133*, 489-521, 1990.

Brace, W. F., and E. G. Bombolakis, A note on brittle crack growth in compression, *J. Geophys. Res., 68, 3709-3713*, 1963.

Brace, W. F., B. W. Paulding, Jr., and C. Scholz, Dilatancy in the fracture of crystalline rocks, *J. Geophys. Res., 71, 3939-3953*, 1966.

Du Y., and A. Aydin, Interaction of multiple cracks and formation of echelon crack arrays, *Int. J. Numer. Anal. Methods Geomech., 15*, 205-218, 1991.

Griffith, A. A., The phenomena of rupture and flow in solids, *Philos. Trans. R. Soc. London A, 221*, 163-198, 1920.

Hadley, K., Dilatancy: Further studies in crystalline rocks, Ph.D. thesis, Mass. Inst. Technol., Cambridge, 1975.

Hallbauer, D. K., H. Wagner, and N. G. W. Cook, Some observations concerning the microscopic and mechanical behavior of quartzite specimens in stiff, triaxial compression tests, *Int. J. Rock Mech. Min. Sci. Geomech. Abstr., 10*, 713-26, 1973.

Horii, H., and S. Nemat-Nasser, Compression-induced microcrack growth in brittle solids: Axial splitting and shear failure, *J. Geophys. Res., 90, 3105-3125*, 1985.

Horii, H., and S. Nemat-Nasser, Brittle failure in compression: splitting, faulting and brittle-ductile transition, *Philos. Trans. R. Soc. London A, 319*, 337-374, 1986.

Jaeger, J. C., and N. G. W. Cook, *Fundamentals of Rock Mechanics*, 3rd ed., 593 pp., Chapman and Hall, London, 1984.

Kranz, R. L., Crack growth and development during creep in Westerly granite, *Int. J. Rock Mech. Min. Sci., 16*, 23-36, 1979.

Lawn, B. R., and T. R. Wilshaw, *Fracture of Brittle Solids*, 204 pp., Cambridge University Press, New York, 1975.

Lockner D. A., and J. D. Byerlee, Precursory AE patterns leading to rock fracture, in *Proceedings, Fifth Conference on Acoustic Emission/Microseismic Activity in Geological Structures and Materials*, edited by H. R. Hardy, Trans-Tech Publ., Clausthal-Zelleerfeld, Germany, 1993.

Lockner, D. A., J. D. Byerlee, V. Kuksenko, A. Ponomarev, and A. Sidrin, Quasi-static fault growth and shear fracture energy in granite, *Nature, 350*, 39-42, 1991.

Lockner D. A., J. D. Byerlee, V. Kuksenko, A. Ponomarev, and A. Sidrin, Observations of quasi-static fault growth from acoustic emissions, in *Fault Mechanics and Transport Properties of Rocks*, edited by B. Evans and T.-f. Wong, 3-31, Academic, San Diego, Calif., 1992a.

Lockner, A. D., Z. Reches, and D. E., Moore, Microcrack Interaction Leading to shear fracture, in *Rock Mechanics, Proceedings of the 33rd U.S. Symposium*, edited by J. R. Tillerson and W. R. Wawersik, pp. 807-816, A. A. Balkema, Rotterdam, Netherlands, 1992b.

Madden, T. R., Microcrack connectivity in rocks: A renormalization group approach to the critical phenomena of conduction and failure in crystalline rocks, *J. Geophys. Res., 88*, 585-592, 1983.

McClintock, F. A. and J. B. Walsh, Friction on Griffith cracks in rocks under pressure, in *Proceedings of the 4th National Congress on Applied Mechanics*, pp. 1015-1021, American Society of Mechanical Engineers, New York, 1962.

Moore, D. E., and A. D. Lockner, The role of microcracking in shear fracture propagation in granite, *J. Struct. Geol.*, in press, 1994.

Moore, D. E., R. Summers, and J. D. Byerlee, Faults, fractures and other deformation features produced during loading of

granite in triaxial equipment, *U.S. Geol. Surv. Open File Rep., 90-349*, 1990.

Peng, S., and A. M. Johnson, Crack growth and faulting in cylindrical specimens of Chemsfold granite, *Int. J. Rock Mech. Min. Sci. Geomech. Abstr., 9*, 37-86, 1972.

Petit, J. P., and M. Barquins, Can natural faults propagate under mode II conditions?, *Tectonics, 7*, 1243-1256, 1988.

Petit, J. P., and M. Barquins, Fault propagation in mode II conditions: Comparison between experimental and mathematical models, applications to natural features, in *Mechanics of Jointed and Faulted Rock*, edited by H. P. Rossmanith, pp. 213-220, A.A. Balkema, Rotterdam, Netherlands,1990.

Pollard, D. D. and P. Segall, Theoretical displacements and stresses near fractures in rock with applications to faults, joints, veins, dikes, and solution surfaces, in *Fracture Mechanics of Rock*, edited by B. K. Atkinson, pp. 277-349, Academic, San Diego, Calif., 1987.

Reches, Z., Evolution of fault patterns in clay experiments, *Tectonophysics, 145*, 141-156, 1988.

Reches, Z., and D. Lockner, Self-organized cracking- A mechanism for brittle faulting (abstract), *Eos Trans. AGU, 71*, 1586, 1990.

Rice, J. R., The mechanics of earthquake rupture, in *Physics of the Earth's Interior*, edited A. M. Dziewonski and E. Boschi, pp. 555-649, North-Holland, New York, 1980.

Sammis, C. G., and M. F. Ashby, The failure of brittle porous solids under compressive stress states, *Acta Metall., 34*, 511-526, 1986.

Scholz, C. H., Microfracturing and the inelastic deformation of rock in compression, *J. Geophys. Res., 73*, 1417-1432, 1968.

Scholz, C. H., J. Z. Yu, and M. H. Anders, Fault process zones: Observations and theory, *Eos Trans. AGU, 74*(16), Spring Meeting Suppl., 295, 1993.

Segall, P., and D. Pollard, Joint formation in granitic rock of the Sierra Nevada, *Geol. Soc. Am. Bull., 94*, 563-575, 1983.

Tapponnier, P., and W. F. Brace, Development of stress-induced microcracks in Westerly granite, *Int. J. Rock Mech. Min. Sci., 13*, 103-113, 1976.

D. A. Lockner, U.S. Geological Survey, 345 Middlefield Road, MS 970, Menlo Park, CA 94025.

Z. Reches, Department of Geology, Hebrew University, Jerusalem 91904, Israel. (e-mail: zreches@geohub.gcn.uoknor.edu)

(Received August 23, 1993; revised December 22, 1993; accepted January 12, 1994.)